

# Tests of general relativity from timing the double pulsar

M. Kramer,<sup>1\*</sup> I.H. Stairs,<sup>2</sup> R.N. Manchester,<sup>3</sup> M.A. McLaughlin,<sup>1,4</sup>  
A.G. Lyne,<sup>1</sup> R.D. Ferdman,<sup>2</sup> M. Burgay,<sup>5</sup> D.R. Lorimer,<sup>1,4</sup>  
A. Possenti,<sup>5</sup> N. D'Amico,<sup>5,6</sup> J.M. Sarkissian,<sup>3</sup> G.B. Hobbs,<sup>3</sup>  
J.E. Reynolds,<sup>3</sup> P.C.C. Freire<sup>7</sup> and F. Camilo<sup>8</sup>

<sup>1</sup>University of Manchester, Jodrell Bank Observatory, Macclesfield, SK11 9DL, UK

<sup>2</sup>Dept. of Physics and Astronomy, University of British Columbia, 6224 Agricultural Road,  
Vancouver, BC V6T 1Z1, Canada

<sup>3</sup>Australia Telescope National Facility, CSIRO, P.O. Box 76, Epping NSW 1710, Australia

<sup>4</sup>Department of Physics, West Virginia University, Morgantown, WV 26505, USA

<sup>5</sup>INAF - Osservatorio Astronomica di Cagliari, Loc. Poggio dei Pini, Strada 54,  
09012 Capoterra, Italy

<sup>6</sup>Universita' degli Studi di Cagliari, Dipartimento di Fisica, SP Monserrato-Sestu km 0.7,  
09042 Monserrato (CA), Italy

<sup>7</sup>NAIC, Arecibo Observatory, HC03 Box 53995, PR 00612, USA

<sup>8</sup>Columbia Astrophysics Laboratory, Columbia University, 550 West 120<sup>th</sup> Street,  
New York, NY 10027, USA

\*To whom correspondence should be addressed; E-mail: mkramer@jb.man.ac.uk

**The double pulsar system, PSR J0737-3039A/B, is unique in that both neutron stars are detectable as radio pulsars. This, combined with significantly higher mean orbital velocities and accelerations when compared to other binary pulsars, suggested that the system would become the best available testbed for general relativity and alternative theories of gravity in the strong-field regime.**

**Here we report on precision timing observations taken over the 2.5 years since its discovery and present four independent strong-field tests of general relativity. Use of the theory-independent mass ratio of the two stars makes these tests uniquely different from earlier studies. By measuring relativistic corrections to the Keplerian description of the orbital motion, we find that the “post-Keplerian” parameter  $s$  agrees with the value predicted by Einstein’s theory of general relativity within an uncertainty of 0.05%, the most precise test yet obtained. We also show that the transverse velocity of the system’s center of mass is extremely small. Combined with the system’s location near the Sun, this result suggests that future tests of gravitational theories with the double pulsar will supersede the best current Solar-system tests. It also implies that the second-born pulsar may have formed differently to the usually assumed core-collapse of a helium star.**

**Introduction.** Einstein’s general theory of relativity (GR) has so far passed all experimental tests with flying colours (1), with the most precise tests achieved in the weak-field gravity conditions of the Solar System (2, 3). However, it is conceivable that GR breaks down under extreme conditions such as strong gravitational fields where other theories of gravity may apply (4). Predictions of gravitational radiation and self-gravitational effects can only be tested using massive and compact astronomical objects such as neutron stars and black holes. Studies of the double-neutron-star binary systems, PSR B1913+16 and PSR B1534+12, have provided the best such tests so far, confirming GR at the 0.2% and 0.7% level, respectively (5, 6)<sup>1</sup>. The recently discovered double pulsar system, PSR J0737-3039A/B, has significantly higher mean

---

<sup>1</sup> Stairs et al. (2002, ref. (6)) find an agreement of their measured values for PSR B1534+12 with GR at the 0.05% level, but the measurement uncertainty on the most precisely measured parameter in the test,  $s$ , is only 0.7%.

orbital velocities and accelerations than either PSR B1913+16 or PSR B1534+12 and is unique in that both neutron stars are detectable as radio pulsars (7, 8).

PSR J0737–3037A/B consists of a 22-ms period pulsar, PSR J0737–3039A (henceforth called A), in a 2.4-hr orbit with a younger 2.7-s period pulsar, PSR J0737–3039B (B). Soon after the discovery of A (7), it was recognised that the orbit’s orientation, measured as the longitude of periastron  $\omega$ , was changing in time with a very large rate of  $\dot{\omega} = d\omega/dt \sim 17^\circ \text{ yr}^{-1}$ , which is four times the corresponding value for the Hulse-Taylor binary, PSR B1913+16 (5). This immediately suggested that the system consists of two neutron stars, a conclusion confirmed by the discovery of pulsations from B (8). The pulsed radio emission from B has a strong orbital modulation, both in intensity and in pulse shape. It appears as a strong radio source only for two intervals, each of about 10-min duration, while its pulsed emission is rather weak or even undetectable for most of the remainder of the orbit (8, 9).

In double-neutron-star systems, especially those having short orbital periods, observed pulse arrival times are significantly modified by relativistic effects which can be modelled in a theory-independent way using the so-called “Post-Keplerian” (PK) parameters (10). These PK parameters are phenomenological corrections and additions to the simple Keplerian description of the binary motion, describing for instance a temporal change in period or orientation of the orbit, or an additional “Shapiro-delay” that occurs due to the curvature of space-time when pulses pass near the massive companion. The PK parameters take different forms in different theories of gravity and so their measurement can be used to test these theories (11, 1). For point masses with negligible spin contributions, GR predicts values for the PK parameters which depend only on the two a priori unknown neutron-star masses and the precisely measurable Keplerian parameters. Therefore measurement of three (or more) PK parameters provides one (or more) tests of the predictive power of GR. For the double pulsar we can also measure the mass ratio of the two stars,  $R \equiv m_A/m_B = x_B/x_A$ . The ability to measure this quantity provides an important

constraint because in GR and other theories this simple relationship between the masses and semi-major axes is valid to at least first post-Newtonian (1PN) or  $(v/c)^2$  order (12, 11).

**Observations.** Timing observations of PSR J0737–3039A/B have been undertaken using the 64-m Parkes radio telescope in New South Wales, Australia, the 76-m Lovell radio telescope at Jodrell Bank Observatory (JBO), UK, and the 100-m Green Bank Telescope (GBT) in West Virginia, USA, between 2003 April and 2006 January.

At Parkes, observations were carried out in bands centred at 680 MHz, 1374 MHz and 3030 MHz. While timing observations were frequent after the discovery of the system, later observations at Parkes were typically conducted every 3-4 weeks, usually covering two full orbits per session. Observations at the GBT were conducted at monthly intervals, with each session consisting of a 5- to 8-hour track (i.e., 2 to 3 orbits of the double pulsar). Typically, the observing frequencies were 820 and 1400 MHz for alternate sessions. Occasionally, we also performed observations at 340 MHz, in conjunction with pulse profile studies to be reported elsewhere. In addition, we conducted concentrated campaigns of five 8-hour observing sessions, all at 820 MHz, in 2005 May and 2005 November. Observations at JBO employed the 76-m Lovell telescope. Most data were recorded at 1396 MHz, while some observing sessions were carried out at the lower frequency of 610 MHz. The timing data obtained at Jodrell Bank represent the most densely sampled dataset but, because of the limited bandwidth, requiring longer integration times per timing point. The Parkes dataset is the longest one available and hence provides an excellent basis for investigation of secular timing terms.

The time-series data of all systems were folded modulo the predicted topocentric pulse period. The adopted integration times were 30 s for pulsar A (180 s for JBO data) and 300 s for pulsar B. For A, these integration times reflect a compromise between producing pulse profiles with adequate signal-to-noise ratio and sufficient sampling of the orbit to detect and resolve

phenomena that depend on orbital phase, such as the Shapiro delay. The integration time for B corresponds to about 108 pulse periods and is a compromise between the need to form a stable pulse profile while resolving the systematic changes seen as a function of orbital phase.

**Timing measurements.** For each of the final profiles, pulse times-of-arrival (TOAs) were computed by correlating the observed pulse profiles with synthetic noise-free templates (see Fig. 1 in (13), cf. ref. (7)). A total of 131,416 pulse TOAs were measured for A while 507 TOAs were obtained for B. For A, the same template was used for all observations in a given frequency band, but different templates were used for widely separated bands. We note that our observations still provide no good evidence for secular evolution of A's profile (15) despite the predictions of geodetic precession. The best timing precision was obtained at 820 MHz with GASP backend (see ref. (13) for details of this and other observing systems) on the GBT, with typical TOA measurement uncertainties for pulsar A of  $18 \mu\text{s}$  for a 30-s integration.

For B, because of the orbital and secular dependence of its pulse profile (9), different templates were also used for different orbital phases and different epochs. A matrix of B templates was constructed, dividing the data set into 3-month intervals in epoch and 5-minute intervals in orbital phase. The results for the 29 orbital phase bins were studied, and it was noticed that, while the profile changes dramatically and quickly during the two prominent bright phases, the profile shape is simpler and more stable at orbital phases when the pulsar is weak. This apparent stability at some orbital phases cannot be attributed to a low signal-to-noise ratio as secular variations in the pulse shape are still evident. Consequently, the orbital phase was divided into five groups of different lengths to which the same template (for a given 3-month interval) was applied as shown in Fig. 2 of (13). In the final timing analysis, data from the two groups representing the bright phases (IV & V in Fig. 2 of (13)) were excluded to minimize the systematic errors caused by the orbital profile changes. Also, because of signal-to-noise and radio inter-

ference considerations, only data from Parkes and the GBT BCPM backend were used in the B timing analysis.

All TOAs were transferred to Universal Coordinated Time (UTC) using the Global Positional System (GPS) to measure offsets of station clocks from national standards and Circular T of the BIPM to give offsets from UTC, and then to the nominally uniform Terrestrial Time TT(BIPM) timescale. These final TOAs were analysed using the standard software package TEMPO (16), fitting parameters according to the relativistic and theory independent timing model of Damour & Deruelle (17, 10). In addition to the DD model, we also applied the “DD-Shapiro” (DDS) model introduced by Kramer et al. (ref. (18)). The DDS model is a modification of the DD model designed for highly inclined orbits. Rather than fitting for the Shapiro parameter  $s$ , the model uses the parameter  $z_s \equiv -\ln(1-s)$  which gives a more reliable determination of the uncertainties in  $z_s$  and hence in  $s$ . We quote the final result for the more commonly used parameter  $s$  and note that its value computed from  $z_s$  is in good agreement with the value obtained from a direct fit for  $s$  within the DD model. Derived pulsar and binary system parameters are listed in Table 1.

In the timing analysis for pulsar B, we used an unweighted fit to avoid biasing the fit toward bright orbital phases. Uncertainties in the timing parameters were estimated using Monte Carlo simulations of fake data sets for a range of TOA uncertainties, ranging from the minimum estimated TOA error to its maximum observed value of about 4 ms. For B, we also fitted for offsets between datasets derived from different templates in the fit since the observed profile changes prevent the establishment of a reliable phase relationship between the derived templates. This precludes a coherent fit across the whole orbit and hence limits the final timing precision for B. It cannot yet be excluded that different parts of B’s magnetosphere are active and responsible for the observed emission at different orbital phases.

In the final fit, we adopted the astrometric parameters and the dispersion measure derived

for A and held these fixed during the fit, since A’s shorter period and more stable profile give much better timing precision than is achievable for B. Except for the semi-major axis which is only observable as the projection onto the plane-of-the-sky  $x_B = (a_B/c) \sin i$ , where  $i$  is the orbital inclination angle, we also adopted A’s Keplerian parameters (with  $180^\circ$  added to  $\omega_A$ ) and kept these fixed. We also adopted the PK parameter  $\dot{\omega}$  from the A fit since logically this must be identical for the two pulsars; this equality therefore does not implicitly make assumptions about the validity of any particular theory of gravity (see next section). The same applies for  $\dot{P}_B$ . In contrast, the PK parameters  $\gamma$ ,  $s$  and  $r$  are asymmetric in the masses and their values and interpretations differ for A and B. In practical terms, the relatively low timing precision for B does not require the inclusion of  $\gamma$ ,  $s$ ,  $r$  or  $\dot{P}_B$  in the timing model. We can however independently measure  $\dot{\omega}_B$ , obtaining a value of  $16.96 \pm 0.05 \text{ deg yr}^{-1}$ , consistent with the more accurately determined value for A.

Since the overall precision of our tests of GR is currently limited by our ability to measure  $x_B$  and hence the mass ratio  $R \equiv m_A/m_B = x_B/x_A$  (see below), we adopted the following strategy to obtain the best possible accuracy for this parameter. We used the whole TOA data set for B in order to measure B’s spin parameters  $P$  and  $\dot{P}$ , given in Table 1. These parameters were then kept fixed for a separate analysis of the concentrated 5-day GBT observing sessions at 820 MHz. On the timescale of the long-term profile evolution of B, each 5-day session represents a single-epoch experiment and hence requires only a single set of profile templates. The value of  $x_B$  obtained from a fit of this parameter only to the two 5-day sessions is presented in Table 1.

Because of the possible presence of unmodelled intrinsic pulsar timing noise and because not all TOA uncertainties are well understood, we adopt the common and *conservative* pulsar-timing practice of reporting twice the parameter uncertainties given by TEMPO as estimates of the  $1\text{-}\sigma$  uncertainties. While we believe that our real measurement uncertainties are actually

somewhat smaller than quoted, this practice facilitates the comparison with previous tests of GR using pulsars. The timing model also includes timing offsets between the datasets for the different instruments represented by the entries in Table 1 in (13). The final weighted rms post-fit residual is  $54.2\mu\text{s}$ . In addition to the spin and astrometric parameters, the Keplerian parameters of A’s orbit and five PK parameters, we also quote a tentative detection of a timing annual parallax which is consistent with the dispersion-derived distance. Further details are given in ref. (13).

**Tests of general relativity.** Previous observations of PSR J0737–3039A/B (7, 8) resulted in the measurement of  $R$  and four PK parameters: the rate of periastron advance  $\dot{\omega}$ , the gravitational redshift and time dilation parameter  $\gamma$ , and the Shapiro-delay parameters  $r$  and  $s$ . Compared to these earlier results, the measurement precision for these parameters from PSR J0737–3039A/B has increased by up to two orders of magnitude. Also, we have now measured the orbital decay,  $\dot{P}_b$ . Its value, measured at the 1.4% level after only 2.5 years of timing, corresponds to a shrinkage of the pulsars’ separation at a rate of 7mm per day. Therefore, we have measured five PK parameters for the system in total. Together with the mass ratio  $R$ , we have six different relationships that connect the two unknown masses for A and B with the observations. Solving for the two masses using  $R$  and a one PK parameter, we can then use each further PK parameter to compare its observed value with that predicted by GR for the given two masses, providing four independent tests of GR. Equivalently, one can display these tests elegantly in a “mass-mass” diagram (Fig. 1). Measurement of the PK parameters gives curves on this diagram that are in general different for different theories of gravity but which should intersect in a single point, i.e., at a pair of mass values, if the theory is valid (11).

As shown in Fig. 1, we find that all measured constraints are consistent with GR. The most precisely measured PK parameter currently available is the precession of the longitude



of periastron,  $\dot{\omega}$ . We can combine this with the theory-independent mass ratio  $R$  to derive the masses given by the intersection region of their curves:  $m_A = 1.3381 \pm 0.0007 M_\odot$  and  $m_B = 1.2489 \pm 0.0007 M_\odot$ .<sup>2</sup> Table 2 lists the resulting four independent tests that are currently available. All of them rely on comparison of our measured values of  $s$ ,  $r$ ,  $\gamma$  and  $\dot{P}_b$  with predicted values based on the masses defined by the intersection of the allowed regions for  $\dot{\omega}$  and  $R$  in the  $m_A$ - $m_B$  plane. The calculation of the predicted values is somewhat complicated by the fact that the orbit is nearly edge-on to the line of sight, so that the formal intersection region actually includes parts of the plane disallowed by the Keplerian mass functions of both pulsars (see Fig. 1). To derive legitimate predictions for the various parameters, we used the following Monte Carlo method. A pair of trial values for  $\dot{\omega}$  and  $x_B$  (and hence  $R$  and the B mass function) is selected from gaussian distributions based on the measured central values and uncertainties. (The uncertainty on  $x_A$  is very small and is neglected in this procedure.) This pair of trial values is used to derive trial masses  $m_A$  and  $m_B$ , using the GR equation  $\dot{\omega} = 3(\frac{P_b}{2\pi})^{-5/3}(T_\odot M)^{2/3}(1 - e^2)^{-1}$ , where  $M = m_A + m_B$  and  $T_\odot \equiv GM_\odot/c^3 = 4.925490947 \mu\text{s}$ , and the mass-ratio equation  $m_A/m_B = x_B/x_A$ . If this trial mass pair falls in either of the two disallowed regions (based on the trial mass function for  $B$ ) it is discarded. This procedure allows for the substantial uncertainty in the B mass function. Allowed mass pairs are then used to compute the other PK parameters, assuming GR. This procedure is repeated until large numbers of successful trials have accumulated. Histograms of the PK predictions are used to compute the expectation value and 68% confidence ranges for each of the parameters. These are the values given in Table 2.

The Shapiro delay shape illustrated in Fig. 2 gives the most precise test, with  $s_{\text{obs}}/s_{\text{pred}} =$

---

<sup>2</sup>The true masses will deviate from these values by an unknown, but essentially constant, Doppler factor, probably of order  $10^{-3}$  or less (10). Moreover, what is measured is a product containing Newton's gravitational constant  $G$ . The relative uncertainty of  $G$  of  $1.5 \times 10^{-4}$  limits our knowledge of any astronomical mass in kilograms but since the product  $T_\odot = GM_\odot/c^3 = 4.925490947 \mu\text{s}$  is known to very high precision, masses can be measured precisely in solar units.

$0.99987 \pm 0.00050$ .<sup>3</sup> This is by far the best available test of GR in the strong-field limit, having a higher precision than the test based on the observed orbit decay in the PSR B1913+16 system with a 30-year data span (19). As for the PSR B1534+12 system (6), the PSR J0737–3039A/B Shapiro-delay test is complementary to that of B1913+16 since it is not based on predictions relating to emission of gravitational radiation from the system (20). Most importantly, the four tests of GR presented here are qualitatively different from all previous tests because they include one constraint ( $R$ ) that is independent of the assumed theory of gravity at the 1PN order. As a result, for any theory of gravity, the intersection point is expected to lie on the mass ratio line in Fig. 1. GR also passes this additional constraint.

In estimating the final uncertainty of  $x_B$  and hence of  $R$ , we have considered that geodetic precession will lead to changes to the system geometry and hence changes to the aberration of the rotating pulsar beam. The effects of aberration on pulsar timing are usually not separately measurable but are absorbed into a redefinition of the Keplerian parameters. As a result, the *observed* projected sizes of the semi-major axes,  $x_{A,B}^{\text{obs}}$ , differ from the *intrinsic sizes*,  $x_{A,B}^{\text{int}}$  by a factor  $(1 + \epsilon_{A,B}^A)$ . The quantity  $\epsilon_A$  depends for each pulsar A and B on the orbital period, the spin frequency, the orientation of the pulsar spin and the system geometry (11). While aberration should eventually become detectable in the timing, allowing the determination of a further PK parameter, at present it leads to an undetermined deviation of  $x^{\text{obs}}$  from  $x^{\text{int}}$ , where the latter is the relevant quantity for the mass ratio. The parameter  $\epsilon_{A,B}^A$  scales with pulse period and is therefore expected to be two orders of magnitude smaller for A than for B. However, because of the high precision of the A timing parameters, the derived value  $x_A^{\text{obs}}$  may already be significantly affected by aberration. This has (as yet) no consequences for the mass ratio  $R = x_B^{\text{obs}}/x_A^{\text{obs}}$ , as the uncertainty in  $R$  is dominated by the much less precise  $x_B^{\text{obs}}$ . We can explore the likely aberration corrections to  $x_B^{\text{obs}}$  for various possible geometries. Using a range

---

<sup>3</sup> Note,  $s$  has the same relative uncertainty as our determination of the masses.

of values given by studies of the double pulsar’s emission properties (21), we estimate  $\epsilon_A^A \sim 10^{-6}$  and  $\epsilon_B^A \sim 10^{-4}$ . The contribution of aberration therefore is at least one order of magnitude smaller than our current timing precision. In the future this effect may become important, possibly limiting the usefulness of  $R$  for tests of GR. If the geometry cannot be independently determined, we could use the observed deviations of  $R$  from the value expected within GR to determine  $\epsilon_B^A$  and hence the geometry of B.

**Space motion and inclination of the orbit.** Because the measured uncertainty in  $\dot{P}_b$  decreases approximately as  $T^{-2.5}$ , where  $T$  is the data span, we expect to improve our test of the radiative aspect of the system to the 0.1% level or better in about five years’ time. For the PSR B1913+16 and PSR B1534+12 systems, the precision of the GR test based on the orbit-decay rate is severely limited both by the uncertainty in the differential acceleration of the Sun and the binary system in the Galactic gravitational potential and the uncertainty in pulsar distance (22, 6). For PSR J0737–3039A/B, both of these corrections are very much smaller than for these other systems. Based on the measured dispersion measure and a model for the Galactic electron distribution (23), PSR J0737–3039A/B is estimated to be about 500 pc from the Earth. From the timing data we have measured a marginally significant value for the annual parallax,  $3 \pm 2$  mas, corresponding to a distance of 200 – 1000 pc (Table 1), which is consistent with the dispersion-based distance that was also used for studies of detection rates in gravitational wave detectors (7). The observed proper motion of the system (Table 1) and differential acceleration in the Galactic potential (24) then imply a kinematic correction to  $\dot{P}_b$  at the 0.02% level or less. Independent distance estimates also can be expected from measurements of the annual parallax by Very Long Baseline Interferometry (VLBI) observations, allowing a secure compensation for this already small effect. A measurement of  $\dot{P}_b$  at the 0.02% level or better will provide stringent tests for alternative theories of gravity. For example, limits on some scalar-tensor

theories will surpass the best current Solar-system tests (25).

In GR, the parameter  $s$  can be identified with  $\sin i$  where  $i$  is the inclination angle of the orbit. The value of  $s$  given in Table 1 corresponds to  $i = 88^\circ.69_{-0^\circ.76}^{+0^\circ.50}$ . Based on scintillation observations of both pulsars over the short time interval when A is close to superior conjunction, Coles et al. (26) derived a value for  $|i - 90^\circ|$  of  $0^\circ.29 \pm 0^\circ.14$ . This is consistent with our measurement only at the  $3\text{-}\sigma$  level. As mentioned above, we used the DDS model to solve for the Shapiro delay. Fig. 3 shows the resulting  $\chi^2$  contours in the  $z_s - m_B$  plane. The value and uncertainty range for  $s$  quoted in Table 1 correspond to the peak and range of the 68% contour. Because of the non-linear relationship between  $z_s$  and  $s$ , the uncertainty distribution in  $s$  (and hence in  $i$ ) corresponding to these contours is very asymmetric with a very steep edge on the  $90^\circ$  side. Only close to the 99% confidence limit is the timing result consistent with the scintillation-derived value of  $|i - 90^\circ|$  of  $0^\circ.29 \pm 0^\circ.14$  (26). We note that the scintillation measurement is based on the correlation of the scintillation fluctuations of A and B over the short interval when A is close to superior conjunction (i.e., behind B). In contrast, the measurement of  $i$  from timing measurements depends on the detection of significant structure in the post-fit residuals after a portion of the Shapiro delay is absorbed in the fit for  $x_A$  (27). As shown in Fig. 2, the Shapiro delay has a signature that is spread over the whole orbit and hence can be cleanly isolated. We also examined the effects on the Shapiro delay of using only low- or high-frequency data, and found values of  $s$  consistent withing the errors in each case. The scintillation result is based on the plasma properties of the interstellar medium and may also be affected by possible refraction effects in B's magnetosphere. We believe that the timing result is much less susceptible to systematic errors and is therefore more secure.

Scintillation observations have also been used to deduce the system transverse velocity. Ransom et al. (28) derive a value of  $141 \pm 8.5 \text{ km s}^{-1}$  while Coles et al. (26) obtain  $66 \pm 15 \text{ km s}^{-1}$  after considering the effect of anisotropy in the scattering screen. Both of these values are

in stark contrast to the value of  $10 \pm 1 \text{ km s}^{-1}$  (relative to the Solar system barycentre) obtained from pulsar timing (Table 1). We note that the scintillation-based velocity depends on a number of assumptions about the properties of the effective scattering screen. In contrast, the proper motion measurement has a clear and unambiguous timing signature, although the transverse velocity itself scales with the pulsar distance. Even allowing that unmodelled effects of Earth motion could affect the published scintillation velocities by about  $30 \text{ km s}^{-1}$ , the dispersion-based distance would need to be underestimated by a factor of several to make the velocities consistent. We believe this is very unlikely, particularly as the tentative detection of a parallax gives us some confidence in the dispersion-based distance estimate. Hence, we believe that our timing results for both inclination angle and transverse velocity are less susceptible to systematic errors and are therefore more secure than those based on scintillation.

We note that, with the inclination angle being significantly different from  $90^\circ$ , gravitational lensing effects (29) can be neglected. The implied low space velocity, the comparatively low derived mass for B and the low orbit eccentricity are all consistent with the idea that the B pulsar may have formed by a mechanism different to the usually assumed core-collapse of a helium star (30, 31). A discussion of its progenitor is presented elsewhere (32). We also note that, as expected for a double-neutron-star system, there is no evidence for variation in dispersion measure as a function of orbital phase.

**Future tests.** In contrast to all previous tests of GR, we are now reaching the point with PSR J0737–3037A where expressions of PK parameters to only 1PN order may not be sufficient anymore for a comparison of theoretical predictions with observations. In particular, we have measured  $\dot{\omega}$  so precisely (i.e., to a relative precision approaching  $10^{-5}$ ) that we expect corrections at the 2PN level (12) to be observationally significant within a few years. These corrections include contributions expected from spin-orbit coupling (33, 34). A future determination of the

system geometry and the measurement of two other PK parameters at a level of precision similar to that for  $\dot{\omega}$ , would allow us to measure the moment of inertia of a neutron star for the first time (12, 35). While this measurement is potentially very difficult, a determination of A's moment of inertia to a precision of only 30% would allow us to distinguish between a large number of proposed equations of state for dense matter (36, 37). The double pulsar would then not only provide the best tests of theories of gravity in the strong-field regime as presented here but would also give insight into the nature of super-dense matter.

## References and Notes

1. C. Will, *Living Reviews in Relativity* **4**, 4 (2001).
2. B. Bertotti, L. Iess, P. Tortora, *Nature* **425**, 374 (2003).
3. J. G. Williams, S. G. Turyshev, D. H. Boggs, *Phys. Rev. Lett.* **93**, 261101 (2004).
4. T. Damour, G. Esposito-Farèse, *Phys. Rev. D* **58**, 1 (1998).
5. J. H. Taylor, J. M. Weisberg, *ApJ* **345**, 434 (1989).
6. I. H. Stairs, S. E. Thorsett, J. H. Taylor, A. Wolszczan, *ApJ* **581**, 501 (2002).
7. M. Burgay, *et al.*, *Nature* **426**, 531 (2003).
8. A. G. Lyne, *et al.*, *Science* **303**, 1153 (2004).
9. M. Burgay, *et al.*, *ApJ* **624**, L113 (2005).
10. T. Damour, N. Deruelle, *Ann. Inst. H. Poincaré (Physique Théorique)* **44**, 263 (1986).
11. T. Damour, J. H. Taylor, *Phys. Rev. D* **45**, 1840 (1992).

12. T. Damour, G. Schäfer, *Nuovo Cim.* **101**, 127 (1988).
13. Supporting Online Material
14. M. Kramer, *et al.*, *ApJ* **526**, 957 (1999).
15. R. N. Manchester, *et al.*, *ApJ* **621**, L49 (2005).
16. <http://www.atnf.csiro.au/research/pulsar/tempo>.
17. T. Damour, N. Deruelle, *Ann. Inst. H. Poincaré (Physique Théorique)* **43**, 107 (1985).
18. M. Kramer, *et al.*, *Annalen der Physik* **15**, 34 (2006).
19. J. M. Weisberg, J. H. Taylor, *Binary Radio Pulsars*, F. Rasio, I. H. Stairs, eds. (Astronomical Society of the Pacific, San Francisco, 2005), pp. 25–31.
20. J. H. Taylor, A. Wolszczan, T. Damour, J. M. Weisberg, *Nature* **355**, 132 (1992).
21. M. Lyutikov, *MNRAS* **362**, 1078 (2005).
22. T. Damour, J. H. Taylor, *ApJ* **366**, 501 (1991).
23. J. M. Cordes, T. J. W. Lazio, *NE2001. I. A New Model for the Galactic Distribution of Free Electrons and its Fluctuations* (2002). astro-ph/0207156.
24. K. Kuijken, G. Gilmore, *MNRAS* **239**, 571 (1989).
25. T. Damour, G. Esposito-Farèse, to appear. (2006).
26. W. A. Coles, M. A. McLaughlin, B. J. Rickett, A. G. Lyne, N. D. R. Bhat, *ApJ* **623**, 392 (2005).
27. C. Lange, *et al.*, *MNRAS* **326**, 274 (2001).

28. S. M. Ransom, *et al.*, *ApJ* **609**, L71 (2004).
29. R. R. Rafikov, D. Lai, *Phys. Rev. D* **73**, 063003 (2006).
30. E. Pfahl, S. Rappaport, P. Podsiadlowski, H. Spruit, *ApJ* **574**, 364 (2002).
31. T. Piran, N. J. Shaviv, *Phys. Rev. Lett.* **94**, 051102 (2005).
32. I. H. Stairs, S. E. Thorsett, R. J. Dewey, M. Kramer, C. McPhee, *MNRAS* in press (2006).
33. T. Damour, R. Ruffini, *Academie des Sciences Paris Comptes Rendus Ser. Scie. Math.* **279**, 971 (1974).
34. B. M. Barker, R. F. O'Connell, *ApJ* **199**, L25 (1975).
35. N. Wex, *Class. Quantum Grav.* **12**, 983 (1995).
36. I. A. Morrison, T. W. Baumgarte, S. L. Shapiro, V. R. Pandharipande, *ApJ* **617**, L135 (2004).
37. J. M. Lattimer, B. F. Schutz, *ApJ* **629**, 979 (2005).
38. E. M. Standish, *A&A* **336**, 381 (1998).
39. We thank Thibault Damour and Norbert Wex for useful discussions. The Parkes radio telescope is part of the Australia Telescope which is funded by the Commonwealth of Australia for operation as a National Facility managed by CSIRO. The National Radio Astronomy Observatory is a facility of the U.S. National Science Foundation operated under cooperative agreement by Associated Universities, Inc. GASP is funded by an NSERC RTI-1 grant to IHS and by US NSF grants to Donald Backer and David Nice. We thank Paul Demorest, Ramachandran and Joeri van Leeuwen for their contributions to GASP hardware and software development. IHS holds an NSERC UFA, and pulsar research at UBC is supported by



an NSERC Discovery Grant. MB, AP and ND'A acknowledge financial support from the Italian Ministry of University and Research (MIUR) under the national program *Cofin 2003*. FC is supported by NSF, NASA, and NRAO.

with an inset showing an expanded view of the region of principal interest.

**Fig. 1.** The tests of general relativity parameter summarized in a graphical form. Constraints on the masses of the two stars (A and B) in the PSR J0737–3039A/B binary system. Shaded regions are forbidden by the individual mass functions of A and B since  $\sin i$  must be  $\leq 1$ . Other constraining parameters are shown as pairs of lines, where the separation of the lines indicates the measurement uncertainty. For the diagonal pair of lines labelled as  $R$ , representing the mass ratio derived from the measured semi-major axes of the A and B orbits, the measurement precision is so good that the line separation only becomes apparent in the enlarged inset, showing an expanded view of the region of principal interest. The other constraints shown are based on the measured post-Keplerian (PK) parameters interpreted within the framework of general relativity. The PK parameter  $\dot{\omega}$  describes the relativistic precession of the orbit,  $\gamma$  combines gravitational redshift and time dilation, while  $\dot{P}_b$  represents the measured decrease in orbital period due to the emission of gravitational waves. The two PK parameters  $s$  and  $r$  reflect the observed Shapiro delay, describing a delay that is added to the pulse arrival times when propagating through the curved space-time near the companion. The intersection of all line pairs is consistent with a single point that corresponds to the masses of A and B. The current uncertainties in the observed parameters determine the size of this intersection area which is marked in blue and which reflects the achieved precision of this test of GR and the mass determination for A and B.

**Fig. 2.** Measurement of a Shapiro delay demonstrating the curvature of space-time. Timing residuals (differences between observed and predicted pulse arrival times) are plotted as a function of orbital longitude and illustrate the Shapiro delay for PSR J0737–3039A. (a) Observed timing residuals after a fit of all model parameters given in Table 1 *except* the Shapiro-delay terms  $r$  and  $s$  which were set to zero and not included in the fit. While a portion of the delay is absorbed in an adjustment of the Keplerian parameters, a strong peak at  $90^\circ$  orbital longitude

remains clearly visible. This is the orbital phase of A’s superior conjunction, i.e. when it is positioned behind B as viewed from Earth, so that its pulses experience a delay when moving through the curved space-time near B. The clear detection of structure in the residuals over the whole orbit confirms the detection of the Shapiro delay, which is isolated in (b) by holding all parameters to their best-fit values given in Table 1, except the Shapiro delay terms which were set to zero. The line shows the predicted delay at the centre of the data span. In both cases, residuals were averaged in  $1^\circ$  bins of longitude.

**Fig. 3.** Contour plots of the  $\chi^2$  distribution in the plane of the Shapiro-delay parameter  $z_s \equiv -\ln(1 - s)$  and the mass of the B pulsar,  $m_B$ . The contours correspond to 68%, 95% and 99% confidence limits.

Table 1: Parameters for PSR J0737–3039A (A) and PSR J0737–3039B (B). The values were derived from pulse timing observations using the DD (10) and DDS (18) models of the timing analysis program TEMPO and the Jet Propulsion Laboratory DE405 planetary ephemeris (38). Estimated uncertainties, given in parentheses after the values, refer to the least significant digit of the tabulated value and are twice the formal 1- $\sigma$  values given by TEMPO. The positional parameters are in the DE405 reference frame which is close to that of the International Celestial Reference System. Pulsar spin frequencies  $\nu \equiv 1/P$  are in barycentric dynamical time (TDB) units at the timing epoch quoted in Modified Julian Days. The five Keplerian binary parameters ( $P_b$ ,  $e$ ,  $\omega$ ,  $T_0$ , and  $x$ ) are derived for pulsar A. The first four of these (with an offset of  $180^\circ$  added to  $\omega$ ) and the position parameters were assumed when fitting for B’s parameters. Five post-Keplerian parameters have now been measured. An independent fit of  $\dot{\omega}$  for B yielded a value (shown in square brackets) that is consistent with the much more precise result for A. The value derived for A was adopted in the final analysis (see (13)). The dispersion-based distance is based on a model for the interstellar electron density (23).

Timing parameter	PSR J0737–3039A	PSR J0737–3039B
Right Ascension $\alpha$	07 <sup>h</sup> 37 <sup>m</sup> 51 <sup>s</sup> .24927(3)	—
Declination $\delta$	–30°39′40″.7195(5)	—
Proper motion in the RA direction (mas yr <sup>–1</sup> )	–3.3(4)	—
Proper motion in Declination (mas yr <sup>–1</sup> )	2.6(5)	—
Parallax, $\pi$ (mas)	3(2)	—
Spin frequency $\nu$ (Hz)	44.054069392744(2)	0.36056035506(1)
Spin frequency derivative $\dot{\nu}$ (s <sup>–2</sup> )	–3.4156(1) $\times 10^{-15}$	–0.116(1) $\times 10^{-15}$
Timing Epoch (MJD)	53156.0	53156.0
Dispersion measure DM (cm <sup>–3</sup> pc)	48.920(5)	—
Orbital period $P_b$ (day)	0.10225156248(5)	—
Eccentricity $e$	0.0877775(9)	—
Projected semi-major axis $x = (a/c) \sin i$ (s)	1.415032(1)	1.5161(16)
Longitude of periastron $\omega$ (deg)	87.0331(8)	87.0331 + 180.0
Epoch of periastron $T_0$ (MJD)	53155.9074280(2)	—
Advance of periastron $\dot{\omega}$ (deg/yr)	16.89947(68)	[16.96(5)]
Gravitational redshift parameter $\gamma$ (ms)	0.3856(26)	—
Shapiro delay parameter $s$	0.99974(–39, +16)	—
Shapiro delay parameter $r$ ( $\mu$ s)	6.21(33)	—
Orbital period derivative $\dot{P}_b$	–1.252(17) $\times 10^{-12}$	—
Timing data span (MJD)	52760 – 53736	52760 – 53736
Number of time offsets fitted	10	12
RMS timing residual $\sigma$ ( $\mu$ sec)	54	2169
Total proper motion (mas yr <sup>–1</sup> )		4.2(4)
Distance $d(\text{DM})$ (pc)		$\sim 500$
Distance $d(\pi)$ (pc)		200 – 1000
Transverse velocity ( $d = 500$ pc) (km s <sup>–1</sup> )		10(1)
Orbital inclination angle (deg)		88.69(–76, +50)
Mass function ( $M_\odot$ )	0.29096571(87)	0.3579(11)
Mass ratio, $R$		1.0714(11)
Total system mass ( $M_\odot$ )		2.58708(16)
Neutron star mass ( $m_\odot$ )	1.3381(7)	1.2489(7)

Table 2: Four independent tests of GR provided by the double pulsar. The second column lists the observed PK parameters obtained by fitting a DDS timing model to the data. The third column lists the values expected from general relativity given the masses determined from the intersection point of the mass ratio  $R$  and the periastron advance  $\dot{\omega}$ . The last column gives the ratio of the observed to expected value for each test. Uncertainties refer to the last quoted digit and were determined using Monte Carlo methods.

PK parameter	Observed	GR expectation	Ratio
$\dot{P}_b$	1.252(17)	1.24787(13)	1.003(14)
$\gamma$ (ms)	0.3856(26)	0.38418(22)	1.0036(68)
$s$	0.99974(-39,+16)	0.99987(-48,+13)	0.99987(50)
$r$ ( $\mu$ s)	6.21(33)	6.153(26)	1.009(55)

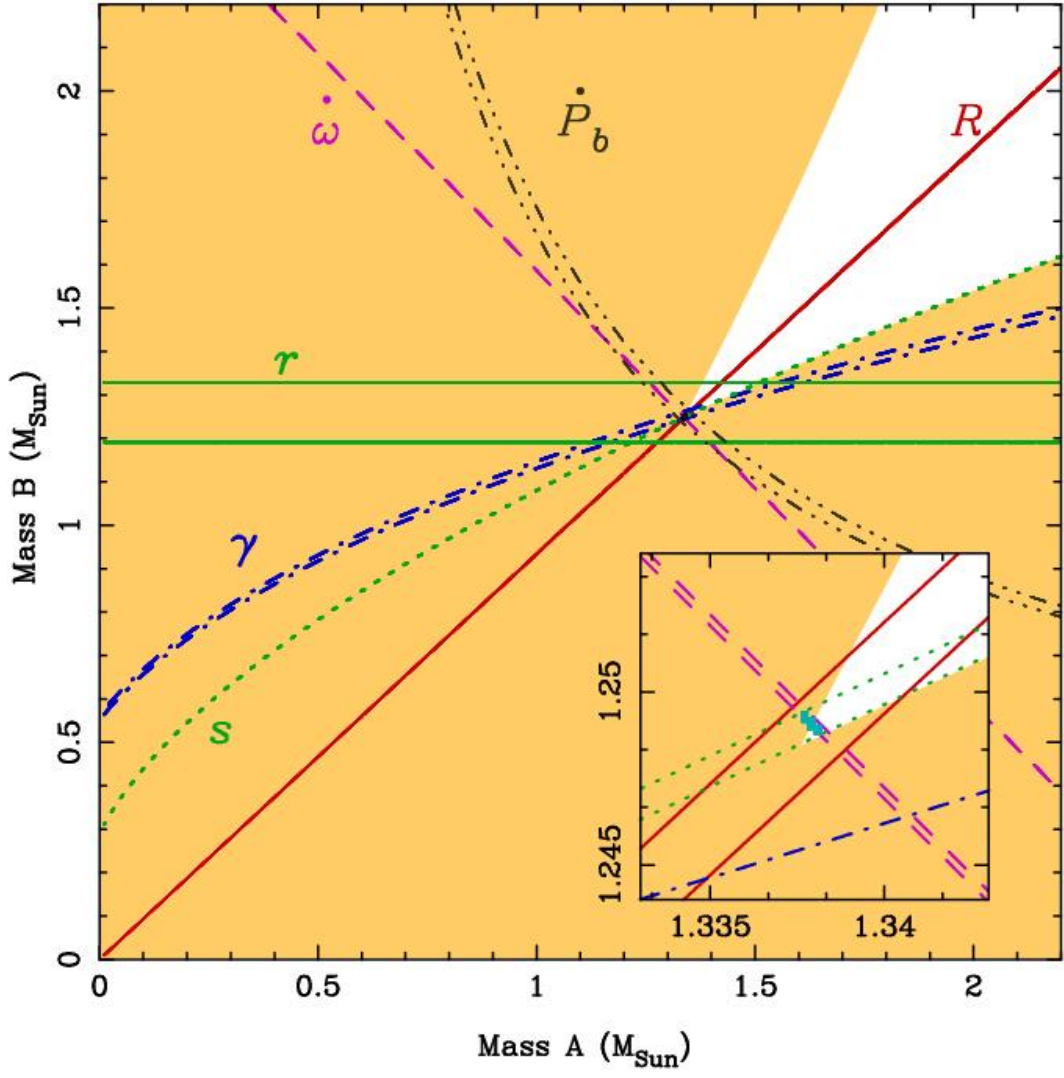


Fig. 1

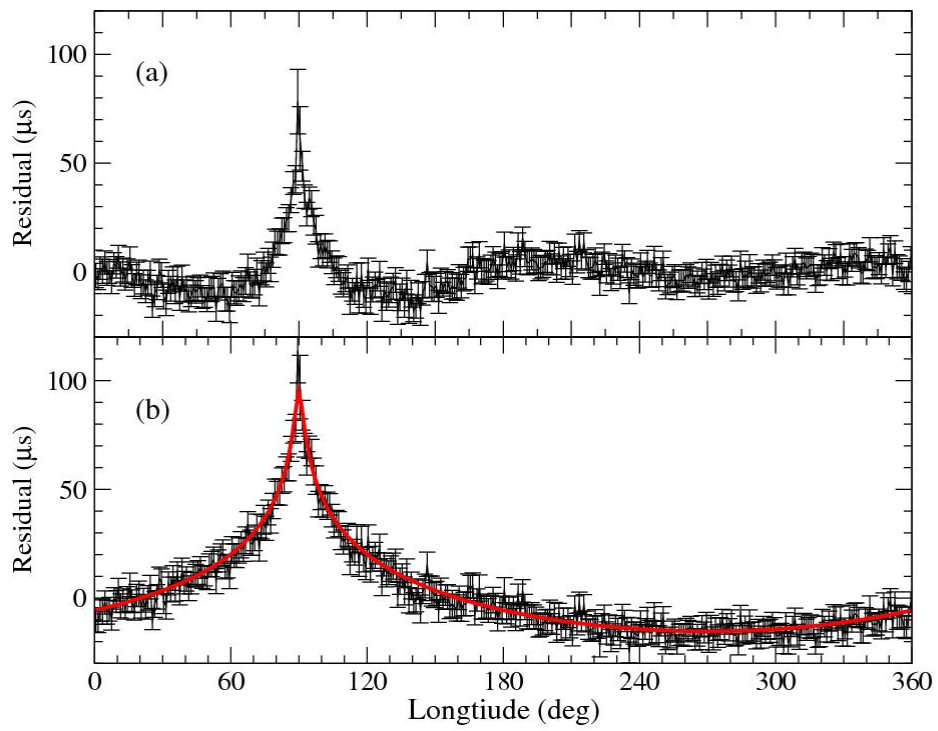


Fig. 2



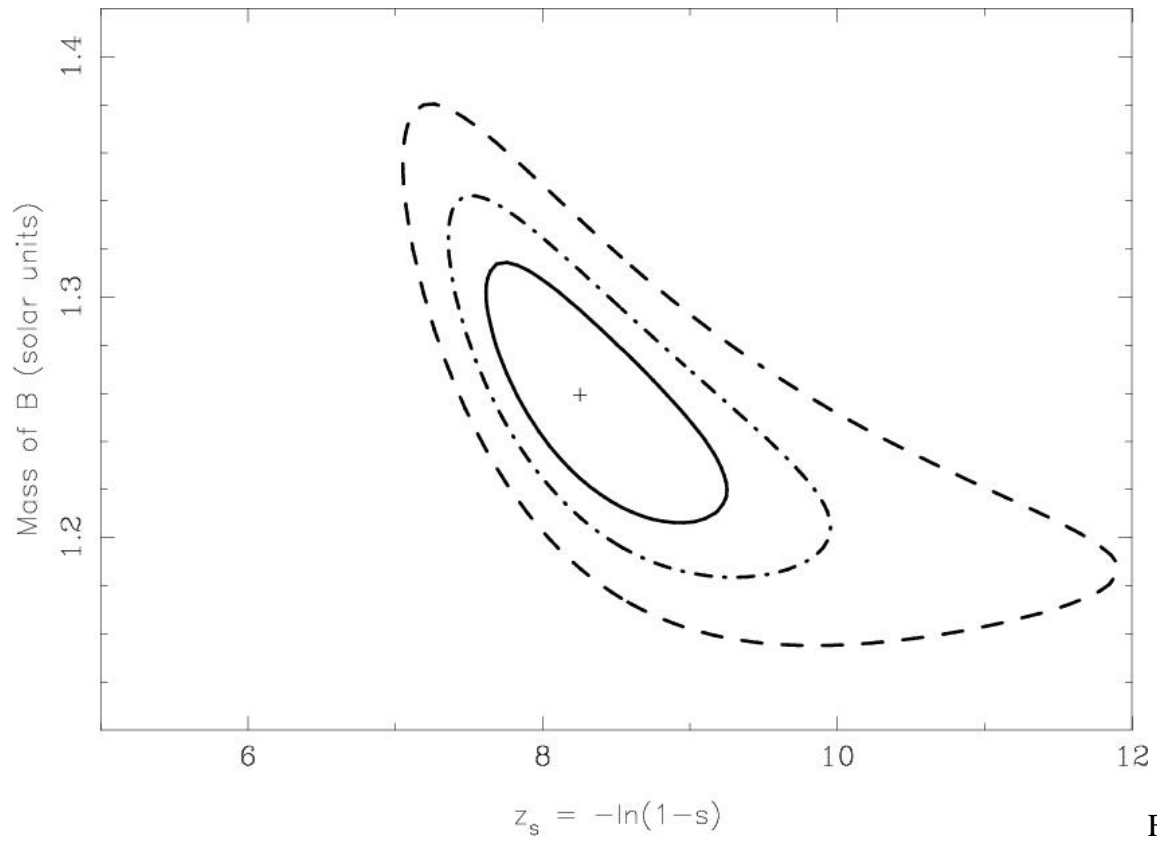


Fig. 3

## Supporting Online Material

### 1 Observing systems

The experimental data presented in the main paper are based on pulsar timing observations at several frequencies between 320 MHz and 3100 MHz using the Parkes radio telescope in Australia, the Lovell radio telescope at Jodrell Bank Observatory, UK, and the Green Bank Telescope (GBT) in the USA, between 2003 April and 2006 January. Details of the observing systems are summarized in Supporting Table 1.

At the Parkes 64-m radio telescope observations were carried out using the centre beam of the 20-cm multibeam receiver and a coaxial 10cm/50cm receiver. For each of these cryogenically cooled receivers, two orthogonally polarized signals were amplified and down-converted to an intermediate frequency. These signals were transferred to band splitters and fed into a filterbank system (FB) for each polarization of each feed. The output of each filter was detected and summed with its corresponding polarization pair. These summed outputs were high-pass filtered and integrated for the sampling interval of  $80 \mu\text{s}$  and then one-bit digitised. While the original frequency channels were folded with a reference frequency corresponding to the band centre, timing was performed on sub-bands.

Observations at the GBT utilized two different data acquisition systems. The Berkeley-Caltech Pulsar Machine (BCPM) is a flexible filterbank system (1), with which we collected 4-bit summed-polarization data. The Green Bank Astronomical Signal Processor (GASP) carries out 8-bit Nyquist-sampling of the incoming dual-polarization signal, after which it performs coherent dedispersion in software on a Linux-based cluster for each of several 4-MHz channels (2, 3). The data stream is then detected, and the two polarizations are usually flux-calibrated before summation using a diode noise source as a reference.

At Jodrell Bank we used an incoherently dedispersing filterbank system. Its parameters are

summarized in Table 1, while details of the observing system can be found in ref. 4.

## 2 Dedispersion

Since the interstellar medium (ISM) is ionized, the propagation speed of radio pulses depends on their radio frequency with pulses emitted at a high radio frequencies arriving earlier than low-frequency pulses. Unless this effect is accounted for, pulses will be broadened over the finite observing bandwidth. Two dedispersion techniques are in use. For “incoherent dedispersion”, the bandwidth is sub-divided into a number of frequency channels which are detected and sampled independently. Dispersion smearing is thereby reduced to the smearing across an individual filterbank channel. The “coherent dedispersion” technique involves the application of an inverse “ISM-filter” to the raw voltage data received from the antenna (5). This technique is computationally more intensive but removes the effects of dispersion completely.

At Parkes and Jodrell Bank we obtained incoherently dedispersed data using the filterbank systems listed in Table 1. The resulting profiles were summed across frequency channels with appropriate delays to remove the effects of interstellar dispersion. For the wide-bandwidth Parkes data, where the original frequency channels were folded with a reference frequency corresponding to the band centre, timing was performed on sub-bands. The number of sub-bands was chosen such that the dispersion delay across the sub-bands was significantly smaller than the overall timing precision. Analysis of TOA data separately for the different sub-bands properly accounts for the fact that data at different frequencies received at a given time correspond to different orbital phases at emission due to the differential dispersion delay (see e.g. (6)).

At the GBT, the BCPM data were divided in four frequency sub-bands, separately dedispersed, folded and timed. In contrast, each GASP 4-MHz channel was coherently dedispersed and folded using the channel centre frequency as a reference. The GASP channels were then summed appropriately to give a single TOA for each integration.

### 3 Pulse Time-of-Arrival analysis

Pulse times-of-arrival (TOAs) were computed by correlating the observed pulse profiles with synthetic noise-free templates (see Figs. 1 and 2; cf. ref. (7)). All datasets obtained at different epochs and frequencies with different data acquisition hardware and telescopes were studied for possible systematic errors and artificial correlations. Firstly, correlations between successive TOAs were investigated by computing the post-fit root-mean-square (rms) timing residuals with averaging of consecutive TOAs, expecting that the rms residual should decrease with the square-root of the number of averaged TOAs. Datasets with significant deviations from this expected scaling were excluded from the analysis. Secondly, for the GBT observations where we recorded data with two different data acquisition systems in parallel, we preferred to use to more accurate GASP data and only used BCPM data if no GASP TOAs were available within 2 minutes of a BCPM TOA. Thirdly, the uncertainties of the TOAs in the remaining datasets were studied by inspecting the reduced  $\chi^2$  achieved in the fit of the timing model. For most datasets we applied a small quadrature addition and a scaling factor to the uncertainties to obtain the expected value of  $\chi_{\text{red}}^2 = 1$ . No adjustments to the TOA uncertainties were needed for the GASP data; this is not surprising as the 8-bit sampling provides excellent profile fidelity. Finally, all retained datasets were combined in a weighted least-squares fit of the DD and DDS models. Following these fits, we verified that the  $\chi_{\text{red}}^2$  for each data subset was still close to unity. A total of 131,416 arrival times were included in the final analysis of A while 507 TOAs were used for B, most at frequencies close to 820 MHz and 1400 MHz. The much smaller number of TOAs for B results from several factors: JBO data were not used, the integration time for B was a factor of ten larger than for A, the data were summed over the entire observed frequency band, only about 20% of the orbit was used and finally, even in the analysed regions, B was often too weak to give a significant TOA. Figures 3 and 4 summarise the TOA distributions for

the different observatories for pulsars A and B respectively. Finally, we present the covariance matrix as computed by TEMPO for the fit of the DDS timing model in Table 2.

## References and Notes

1. D. C. Backer, *et al.*, *PASP* **109**, 61 (1997).
2. P. Demorest, *et al.*, *American Astronomical Society Meeting Abstracts* **205**, (2004).
3. R. D. Ferdman, *et al.*, *American Astronomical Society Meeting Abstracts* **205**, (2004).
4. D. M. Gould, A. G. Lyne, *MNRAS* **301**, 235 (1998).
5. T. H. Hankins, B. J. Rickett, *Methods in Computational Physics Volume 14 — Radio Astronomy* (Academic Press, New York, 1975), pp. 55–129.
6. G. B. Hobbs, R. T. Edwards, R. N. Manchester, *MNRAS* **369**, 655 (2006).
7. M. Kramer, *et al.*, *ApJ* **526**, 957 (1999).

**Supporting Table 1.** Summary of the observing systems used for timing observations of the double pulsar.

Telescope	Instrument	Centre freq. (MHz)	Gain (K/Jy)	$T_{sys}$ (K)	Sample interval ( $\mu$ s)	Bandwidth (MHz)	Number of channels
Parkes	FB	680	0.66	45	80	64	128
		1374	0.74	22	80	256	512
		3030	0.62	28	80	768	256
GBT	BCPM	820	2.0	25	72	48	96
		1400	2.0	20	72	96	96
	GASP	340	2.0	70	0.25	16	4
		820	2.0	25	0.25	64	16 <sup>a</sup>
Jodrell Bank	FB	610	1.1	32	44.4	8	32
		1396	1.1	32	44.4	64	64

<sup>a</sup>The number of channels and hence bandwidth that was used varied occasionally within a given session due to the removal of channels contaminated with radio frequency interference and/or occasional recording disk-space limitations.

**Supporting Table 2.** Covariance matrix as computed by TEMPO for a fit of the DDS timing model to the TOAs of A.

	$\nu$	$\dot{\nu}$	Dec	RA	PMDec	PMRA	$x$	$e$	$T_0$	$P_b$	$\omega$	$\dot{\omega}$	$\gamma$	DM	$\pi$	$\dot{P}_b$	$z_s$	$m_2$	
$\nu$	1.00																		
$\dot{\nu}$	-0.76	1.00																	
Dec	0.16	-0.31	1.00																
RA	0.10	-0.08	0.18	1.00															
PMDec	-0.25	0.39	-0.83	-0.16	1.00														
PMRA	0.01	-0.28	0.04	-0.71	0.12	1.00													
$x$	-0.02	0.02	0.01	0.00	-0.01	-0.01	1.00												
$e$	0.00	0.00	0.01	-0.01	-0.02	-0.01	0.66	1.00											
$T_0$	-0.54	0.43	-0.01	0.02	0.02	-0.03	0.00	0.01	1.00										
$P_b$	0.47	-0.47	0.01	-0.02	-0.02	0.02	-0.15	-0.15	-0.85	1.00									
$\omega$	-0.54	0.42	-0.01	0.02	0.02	-0.03	0.06	0.01	0.99	-0.84	1.00								
$\dot{\omega}$	0.47	-0.48	0.01	-0.02	-0.02	0.02	-0.15	-0.15	-0.85	1.00	-0.84	1.00							
$\gamma$	-0.02	-0.02	0.00	0.01	0.00	0.00	0.44	0.01	-0.03	0.02	0.10	0.03	1.00						
DM	-0.02	0.02	-0.01	0.01	0.03	0.02	0.00	0.00	0.00	0.00	0.00	0.00	0.00	1.00					
$\pi$	0.05	-0.02	-0.21	0.16	0.20	-0.12	-0.03	-0.04	-0.01	-0.01	0.00	-0.01	0.02	-0.02	1.00				
$\dot{P}_b$	0.01	-0.02	0.00	0.03	0.00	-0.02	0.05	0.00	-0.03	-0.06	0.01	0.01	0.13	0.00	-0.01	1.00			
$z_s$	-0.01	0.02	0.01	-0.01	-0.01	0.00	0.55	0.44	0.01	-0.10	0.01	-0.10	-0.01	0.00	-0.01	0.00	1.00		
$m_2$	0.01	-0.03	-0.01	0.00	0.01	0.01	-0.85	-0.75	-0.02	0.18	-0.02	0.18	-0.02	0.00	0.03	0.00	-0.72	1.00	

**Supporting Figure 1.** Pulse profile templates used for TOA determinations for pulsar A.

**Supporting Figure 2.** Regions of orbital phase (hatched) used for timing of pulsar B and pulse profile templates for these phases derived from and used for the 820 MHz GBT observations in May 2005. Each of the template plots covers a range of  $60/360 = 0.17$  in pulse phase. Similar but different templates were used for other frequencies and epochs. While B was clearly detectable in these three regions, it is actually brightest in the two cross-hatched regions, but because the shape of the profile evolves quickly and dramatically in these regions, they were excluded from the timing analysis.

**Supporting Figure 3.** Timing residuals obtained for pulsar A for the three telescopes and their distribution. The upper panel shows the distribution of observations in frequency.

**Supporting Figure 4.** Timing residuals obtained for pulsar B for Parkes and the GBT and their distribution. The upper panel shows the distribution of observations in frequency.



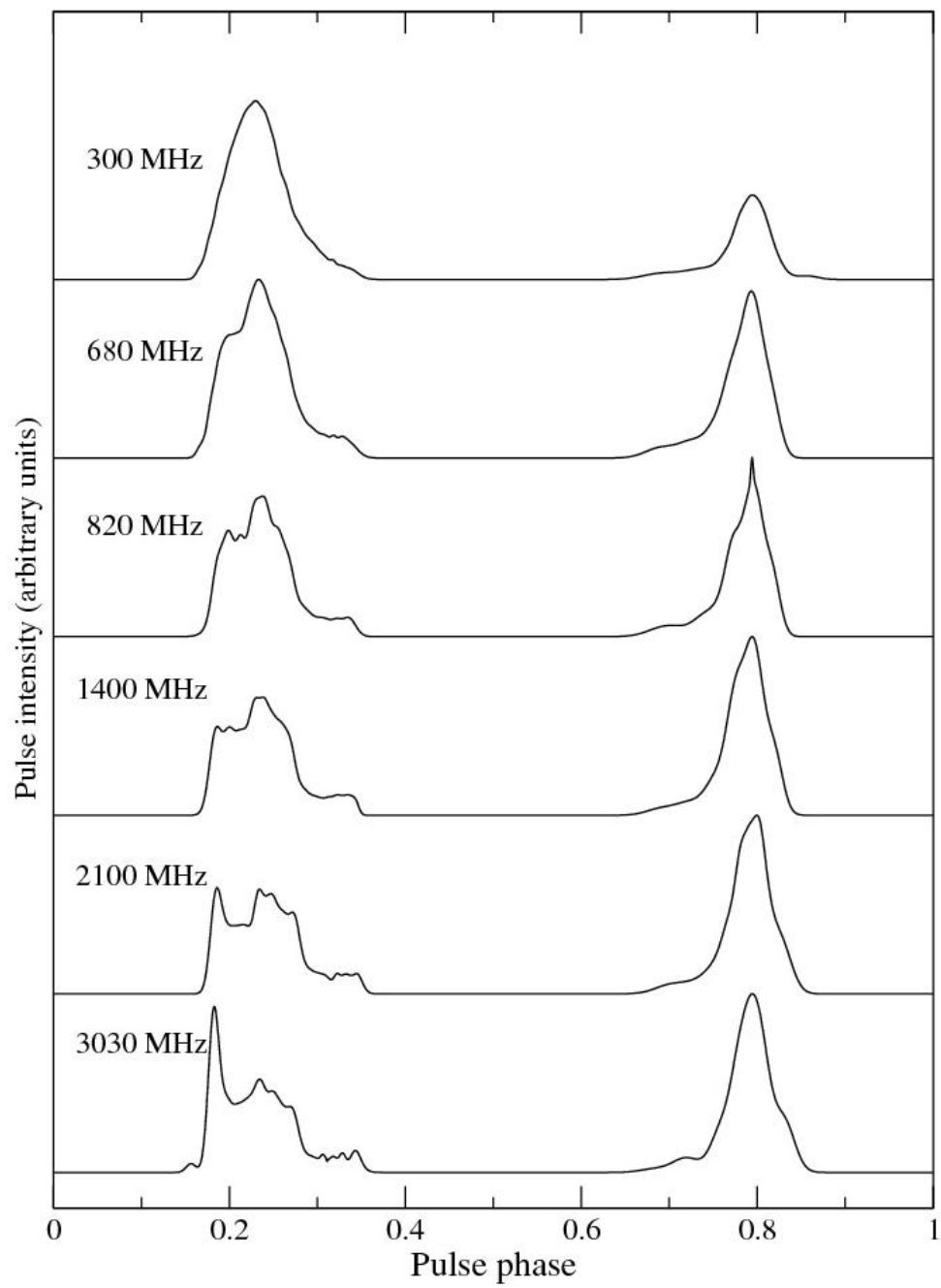


Fig. 1

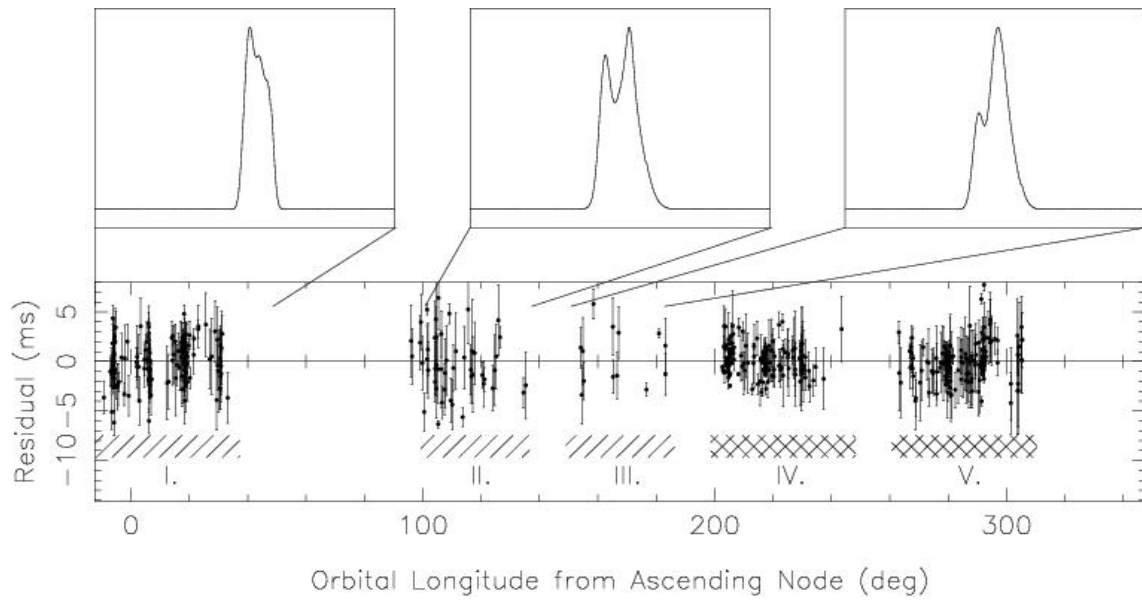


Fig. 2

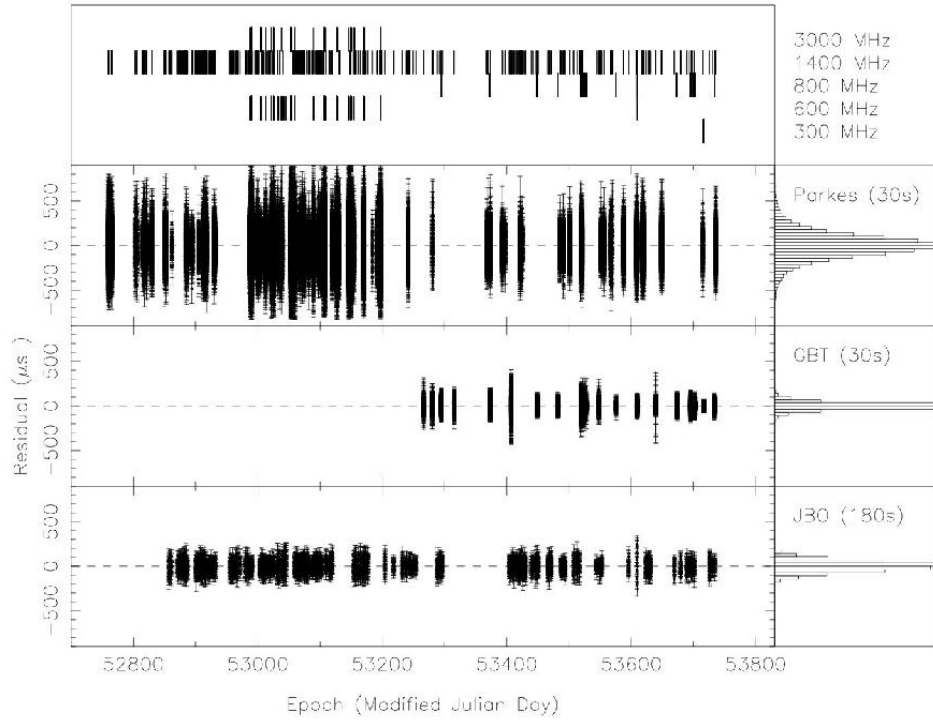


Fig. 3

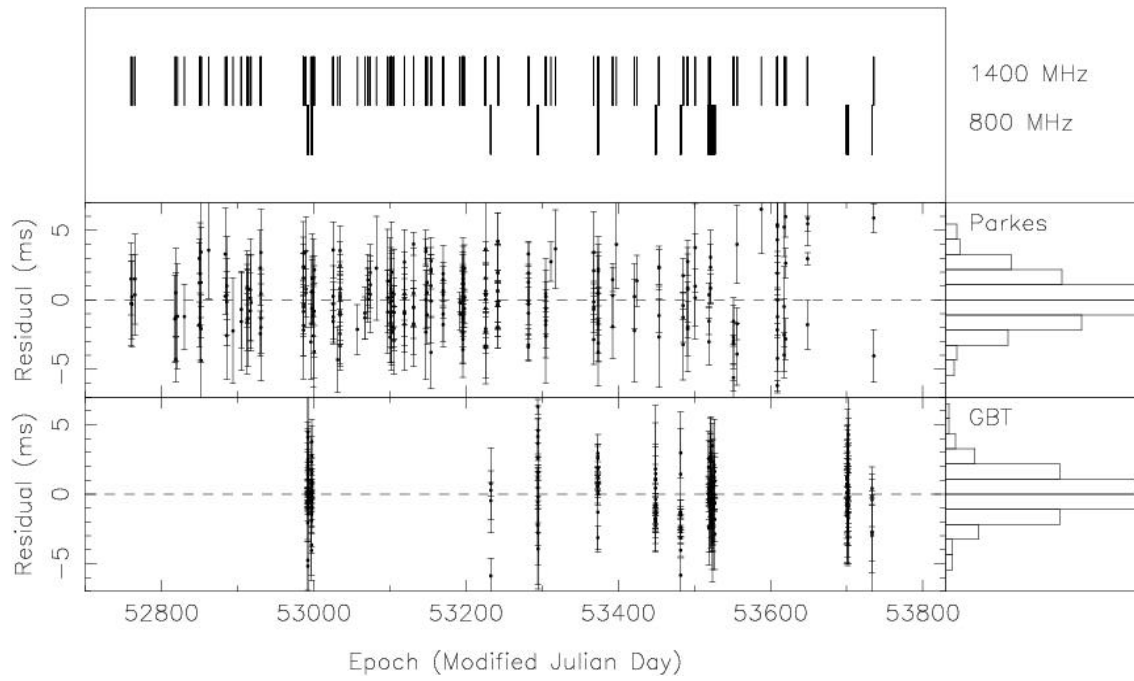


Fig. 4